Characterizing Miniaturized CNT Collimators

for a Wearable Spectrometer

Bridget Kemper

A senior thesis submitted to the faculty of
Brigham Young University
in partial fulfillment of the requirements for the degree of

Bachelor of Science

Robert Davis and Richard Vanfleet, Advisors

Department of Physics and Astronomy

Brigham Young University

ABSTRACT

Characterizing Miniaturized CNT Collimators
for a Wearable Spectrometer

Bridget Kemper
Department of Physics and Astronomy, BYU
Bachelor of Science

Miniaturized spectrometers could enable the application of spectroscopy in wearable devices such as fitness/health monitors. In prior work, miniaturized spectrometers with carbon nanotube parallel-hole collimators were fabricated for use in diffuse light spectroscopy. The miniaturized collimators were formed using carbon nanotube templated microfabrication (CNT-M). CNT-M collimators were grown on an opaque silicon substrate and removed for use. For the CNT-M structure to be robust enough for transfer, it requires significant carbon infiltration. However, this infiltration step results in increased sidewall reflection, impairing the collimation of light. Here we present the use of a transparent fused silica growth substrate. This allows the collimators to remain on the transparent substrate in spectroscopy applications, circumventing the need for infiltration and substrate removal steps. Omitting the carbon infiltration reduced sidewall reflection and improved collimation performance.

Keywords: Micro Elctro Mechanical Systems, Spectroscopy, Light Propagation

ACKNOWLEDGMENTS

I would like to extend thanks to the Physics department for giving me the an environment, space, and resources for research. Along with Octavian Solutions for providing funding for the essentially the entirety of my research.

I'd like to acknowledge the BYU Integrated Microfabrication Lab and the BYU Electron Microscopy Facility for training, support, and equipment access, without which findings wouldn't have been achieved.

I am endebted to my friends, peers, and researchers which endure my senselessness and even help me throughout my academic career. They've taught me so much in both Physics and life.

Lastly, I'd like to thank my advisors Dr Robert Davis and Dr Vanfleet who graciously kept believing and being patient with me.

Contents

List of Figures

Chapter 1

Introduction

Miniaturized spectrometers can be utilized wearable devices, such as fitness and health monitors, by enabling compact and portable spectroscopy applications. Spectrometers are typically are large instruments that sit on tables in labs. For the application of a wearable device our group is looking into spectroscopy to record how light interacts with the blood. Our group can do this with a spectrometer which measure the wavelengths of light that has interacted with the bloodstream. To utilize spectroscopy we previously designed a miniaturized spectrometer that can be used for wearable applications [1].

In previous work, a miniaturized spectrometer was developed for diffuse light spectroscopy utilizing a carbon nanotube (CNT) parallel-hole collimators [1]. The spectrometer consists of a CNT collimator layered on top of a LVF (linear variable filter) which is then layered on top of a photo detector. Light will travel through the CNT collimator before being filtered via wavelength based on the light's position along the LVF. The detector then can determine the wavelength of light based off where along the LVF it has detected light.

For the LVF to properly filter wavelengths the light needs to approach on-axis (perpendicular) to the LVF and parallel to the collimator's walls. Since the LVF relies on path length, incoming off-axis light will have a different path length than if it were on-axis, resulting in the LVF inaccurately filtering light. The CNT collimator blocks light that is not traveling on-axis with the collimator's walls, allowing the LVF to accurately record wavelengths.

Previously collimators were fabricated using carbon nanotube-templated micro fabrication (CNT-M) on an opaque silicon substrate and then removed for use [2]. However, this process required significant carbon infiltration to ensure the robustness of the CNT-M structure, which unfortunately increased sidewall reflection, impairing light collimation.

In this study, we investigate light's interaction with CNT collimators that were infiltrated. We compare the performance of infiltrated collimators to that of pristine collimators grown on a transparent fused-silica substrate. Additionally the pristine CNT collimators eliminate the need for carbon infiltration and substrate removal. Using pristine CNTs utilizes the optical properties of CNT forests as an ultra-black material [3]. We observed a correlation between sample infiltration and sidewall reflection intensity. We analyze the light interaction of collimators with a simulation to better understand how light interacts with the pristine and infiltrated CNT forests. We observed that in filtrated CNT collimators exhibit reflection while pristine CNT collimators exhibit transmission. For the application of a LVF spectrometer the pristine CNT collimators provide more accurate measurements.

Chapter 2

Methods

In section 2.1 we fabricated CNT collimators with the previous infiltration method and a novice approach with a transparent fused silica substrate. In section 2.2 fabricated CNT collimators were then tested for light collimation.

2.1 CNT Fabrication

Collimators were formed on both an opaque silicon substrates and a transparent fused silica substrates as follows. Silicon and fused silica wafers were sputtered with 50nm of Al203 at UHV sputtering. A AZ3330 photoresist layered out a hexagonal pattern with pore sizes of 100 microns across and a hedge width of 4 microns. Four nm of iron was then deposited by a custom built thermal evaporator. For protection additional layer of AZ3330 photo resist was then spun on. This layer protects from silicon particles that may scatter during cleaving.

In order to reveal the patterned iron for CNT growth liftoff was performed. Samples were placed in NMP (N-Methyl-2-pyrrolidone), and agitated in a sonicator for 15 minutes. Afterwards samples were diluted in petri dishes of IPA (isopropyl alcohol) and subsequently mil pore (pure) water with

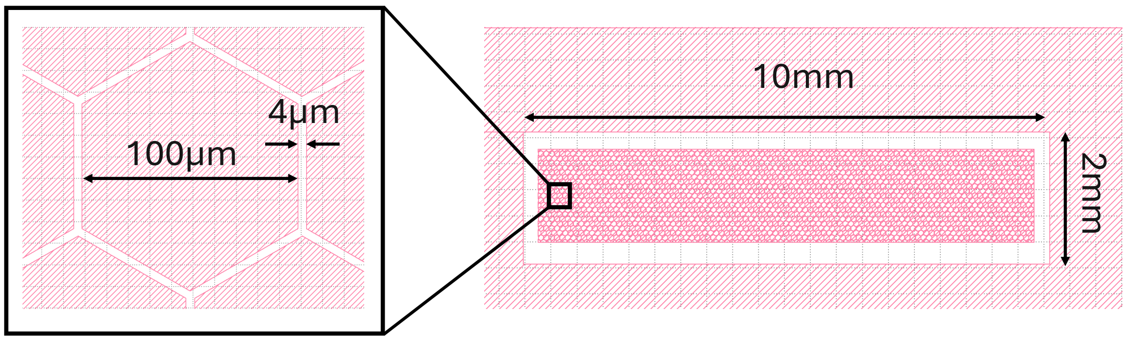

Figure 2.1 CAD of the lithography mask. 100 micron hexagons are separated by 4 micron gaps. The hexagonally patterned region is enclosed by a thick 0.3 mm rectangular border. The pink cross hatch represents where photoresist will remain after patterning. The nanotube growth catalyst (Fe) will remain in the clear region following liftoff. After growth, high-aspect CNT forests will form hexagonally shaped parallel holes connected to a thicker 0.3 mm border.

slight agitation for 2 minutes. Afterwards, samples were blown off with nitrogen to reveal the remaining patterned iron on top of the substrate with the alumina barrier layer.

After liftoff samples are grown via CVD (chemical vapor deposition). Samples on fused silica are heated with a hydrogen flow of 311 sccm. After reaching 750 C, CNT growth is induced with an ethylene flow of 338 sccm and left for a desired growth time, sequentially cooled in argon flowing at 300 sccm, and then removed, these samples are called as-grown samples. Samples on the silicon substrate underwent the initial heating and growth cycle be received an additional infiltration process of a sequential heating immediately after the growth with the same ethylene flow rates at 900 C for 10, 15, and 20 minutes.

After growth samples that underwent the infiltration step had a floor layer of amorphous carbon causing the CNT-structure to have clogged pores. Immediately after infiltration CNT collimators often would begin to delaminate from the substrate and were removed with tweezers. To remove the floor layer, samples were placed with the floor layer facing up and were exposed to an oxygen plasma etch in a Technics Planar Etch II machine. The floor layer of these collimators were removed by incremental 3 minute etches at 200 watts. Samples were inspected after each etch to determine if another etch was needed. These are referred to as infiltrated collimators.

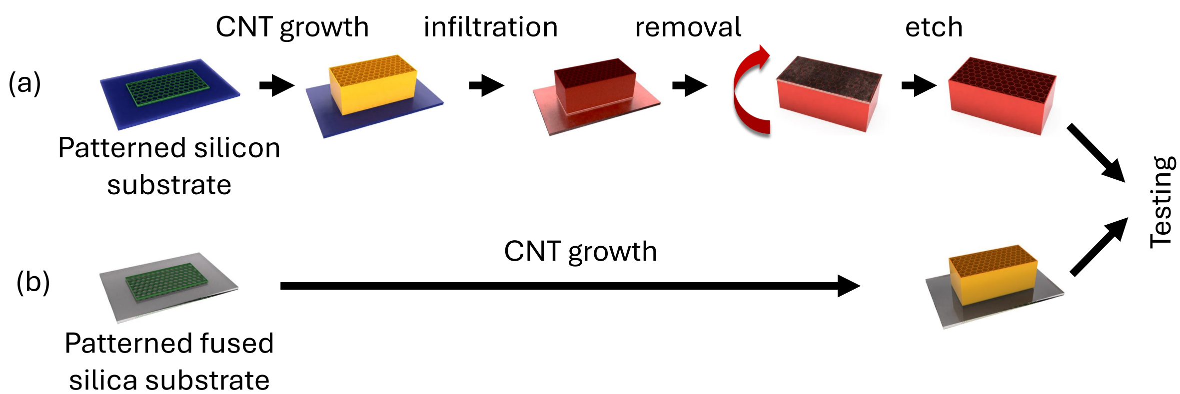

Figure 2.2 Flow chart of CNT collimator fabrication on silicon (a) and fused silica (b).

Bulk density was measured for pristine and 10-min infiltrated CNT collimators. Mass was taken by a Citizen CM21X microbalance. Infiltrated samples were weighed after the oxygen-plasma etch. Sample height was measured by translating the Z axis of an optical microscope from the substrate to the top (canopy) of the CNT forest. Areas were determined by the lithographic pattern of the iron growth catalyst. For pristine collimators, bulk density was calculated from the mass difference before growth (~96229.07222μkg) and after growth (~96380.29445μkg). The area defined by the hexagonal lithography pattern. For infiltrated collimators, mass was measured after the oxygen-plasma etch. Pristine samples had a bulk density of 48.33 ± 11.94 kg/m³, while 10-min infiltrated samples had a bulk density of 500.99 ± 16.05 kg/m³, (the uncertainty is the calculated standard error), consistent with previous results in the group while remaining below the density of graphite [4].

To visually see density increasing with infiltration time SEM images of cross sections of the CNT collimator's walls (see Fig.3.5). Pristine and (5, 10, and 20 minute) infiltrated CNT collimators were cleaved with a razorblade to reveal cross sections of the CNT forest within the collimator walls. The sliced CNT collimators were then imaged in a Verios SEM.

2.2 Mounting and Testing

Samples were prepared,mounted and aligned for optical testing within an optical apparatus to determine how the collimators interacted with light at different angles(see Fig.2.3). After, simple operations normalized data for comparison.

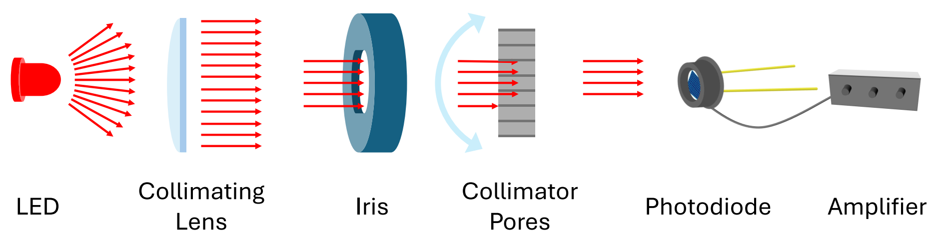

Figure 2.3 Light emitted from a LED is collimated through a lens, sent through an iris to control beam width and block stray light and passes through a CNT collimator as it rotates. Light transmitted through the CNT collimator is then collected by a photo diode.

Without proper alignment data would be skewed. A lateral shift, rotation in azimuthal, or rotation polar angle of the sample relative to the incident light would bias the transmitted intensity toward one side. This bias falsifying the measurement and invalidating comparisons between samples. To combat this, CNT collimators were attached to 3D printed resin mounts coated. The mount covered approximately half of the 0.3 mm border surrounding the hexagonal pattern of the CNT collimator. To prevent light transmitted through the printed piece a thin layer of gold was layered on so light only transmitted through the CNT collimator. Alignment of the CNT collimators was executed by an optical goniometer with two rotational axes ensuring the walls of the parallel hole-collimators were perpendicular to the incoming light. Light intensity could then by reliably measured by a photo diode.

Unpolarized light emitted from an LED was passed through a lens and iris to create a small, collimated beam would pass through the CNT collimator towards a photodiode 150mm away. The collimator was rotated 120° in 0.25° by an electronic stepper motor. The photodiode, connected to a transimpedance amplifier, sent the signal to a LabVIEW MyDAQ, which acquired 10,000 voltage samples per angle point. Data was not dark subtracted as the noise level outside collected data was minimal. A different photodiode was switched out to test CNT collimator's transmission for multiple wavelengths. Photodiodes with wavelengths of 465, 527, 590, 623, and 940nm have spectral bandwidths of 20, 20, 40, 15, and 45nm, respectively.

Chapter 3

Results

Section 3.1 provides data on the collimator's density. Section 3.2 shows SEM images cross-sections of CNT collimator walls. In section 3.3 covers transmitted light intensity of CNT collimators tested in the above apparatus (see Fig. 2.3).

3.1 Collimator Collimation Competence

Transmission data underwent simple data transformations in python. Initially, recorded light transmission was collected in a 120° span. The maximum transmission, when the collimator was parallel with the incident light beam, was at approximately 0. To correct this off-shift, data sets were x-shifted so 0 degrees sits directly at the maximum. Additionally, data sets were normalized. This allowed for comparison between different collimators when regardless of throughput and alignment.

The slope resulting from transmission(see Fig.3.1, 3.2, 3.3) reflect the CNT collimator's geometry. At zero degrees, the collimator's pores are parallel with the beam and light intensity is at it's highest. When rotated the beam begins to be cut off by the collimator walls, decreasing the transmission. How quickly the transmission is cut off relies on the collimator's height, patterning, and characteristics of the CNTs.

In Fig.3.1 the transmission for collimators with varying infiltration times were plotted for comparison. The scale is logarithmic since features are appear at low signal a logarthic scale exaggerates these features. All collimators have a similar main peak around 0 degrees because they have the same pore-height ratio, all collimators have a pore size of __ and heights of __. The infiltrated collimators have secondary peaks where the intensity increases around 20 degrees, while the pristine collimator's transmission slowly decreases.

3.1.1 Light Interaction of CNT Collimators

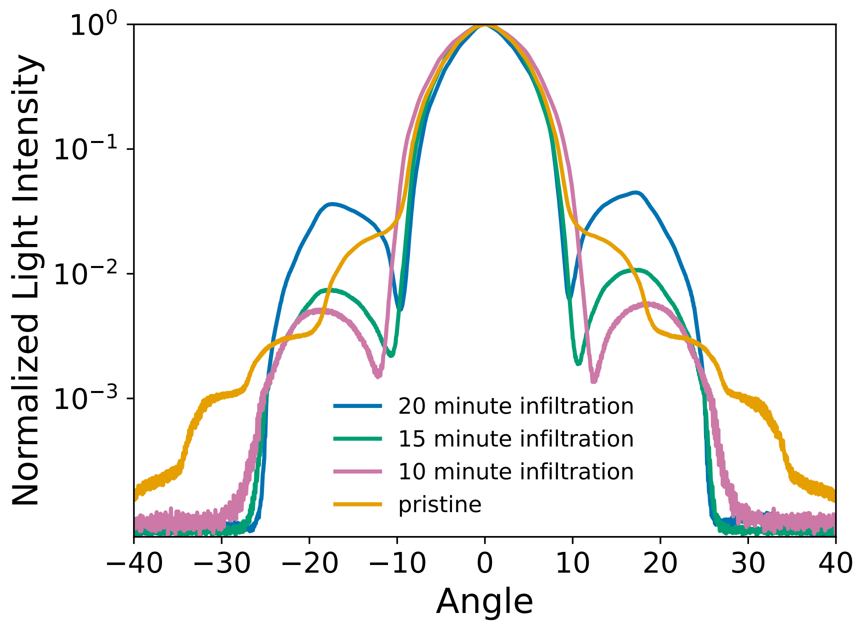

Figure 3.1 Transmitted intensity of unpolarized 623nm light through an individual pristine and infiltrated CNT collimators as a function of incident angle.

3.1.2 Light Collimation of CNT Collimators for multiple wavelengths

Since CNT properties change depending on wavelength, transmission was measured with different LEDs. In fig.3.2 a pristine collimator was tested for a variety of wavelgths in visible light. All lines display the same shape as in the previous figure, fig.3.1, but the rate at which off-axis light is cutoff is different. As wavelength decreases, the collimator becomes better at removing off-axis light. (I'm unsure if I should keep this sentence) The 465nm light/blue curve is reduced to 10^{-3} at 20 degrees, while 623nm light/the pink curve reaches 10^{-3} at 40 degrees.

The collimator with 15-minute infiltration was tested for transmission with the same wavelengths as the pristine collimator (Fig. 3.3). It too has shorter wavelengths have their off-axis light be cut down faster than longer wavelengths. Outside 30 degrees the transmission settles at different intensities. The blue and green curve stop moving around 10^{-3} while other curves are lower. These different intensities are the background noise of the photodiode. Because different LEDs had different brightnesses, the maximum voltage measured by the photodiode was different between measurements. This resulted in the background voltage being different after normalization.

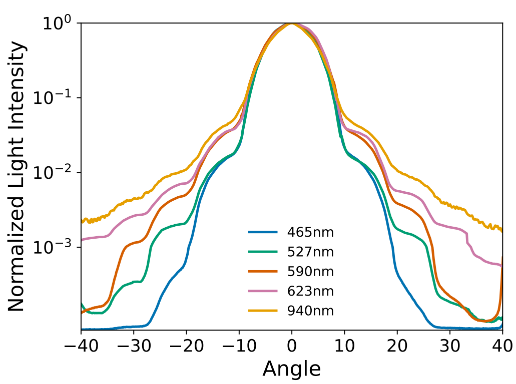

Figure 3.2 Transmission of 465, 527, 590, 623, and 940nm light through a pristine CNT collimator (no infiltration).

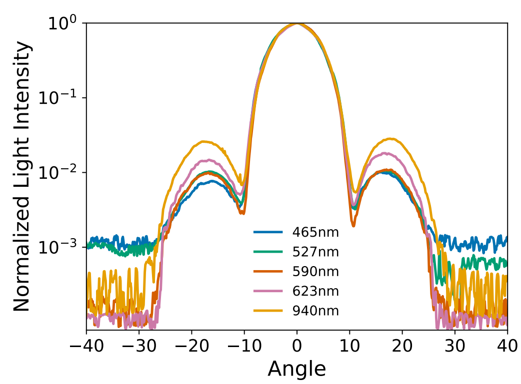

Figure 3.3 Transmission of 465, 527, 590, 623, and 940nm light through a 15-min infiltrated collimator.

3.2 Density

Motivation for why density was taken? Bulk density is seen to increase, which makes sense looking between density and CNT cross sections. Our group has previously measured densities, however carbon nanotube growth is very sensitive to growth parameters. Growths in the our group change with simple variation of placement in furnace, age of gases and equipment changes. The simple definition of infiltration time isn't a reliable measure of CNT property. So bulk density was measured to better assess the CNT material.

It is seen that bulk CNT increases with infiltration time. The infiltration was done at 900C.

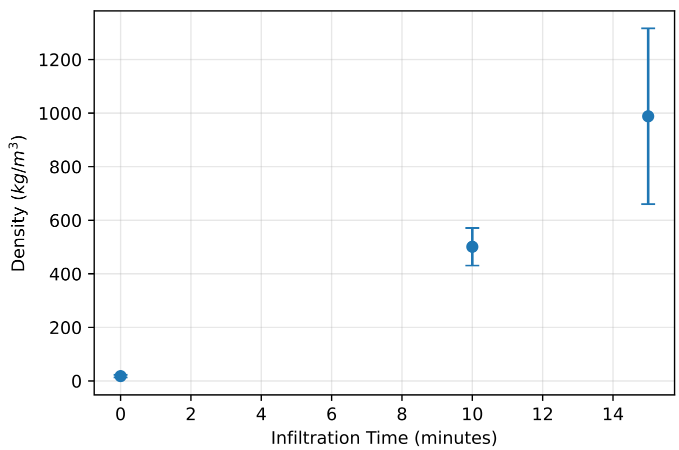

Figure 3.4 Bulk density of CNT collimators increasing with infiltration time. Error bars are the uncertainty is the calculated standard error.

3.3 SEM images

Visually assessing the CNT cross section at different infiltration times allows us to determine that density increases. Within Fig.3.5, the column on the left side gives a better understanding to the 3D collimator geometry. The 4 images on the right show a cross section of the upper part of a hedge that surrounds a pore in the CNT collimator. The white lines in the no infiltration image are each a multi-walled carbon nanotube, each collimator is made of millions of individual CNTs. The no infiltration (pristine) CNT hedge has a wispy cross section, highlighting the ultra low density of CNT forests. All other cross sections with infiltration are visually denser, with the carbon infiltration filling up the area in between the CNTs.

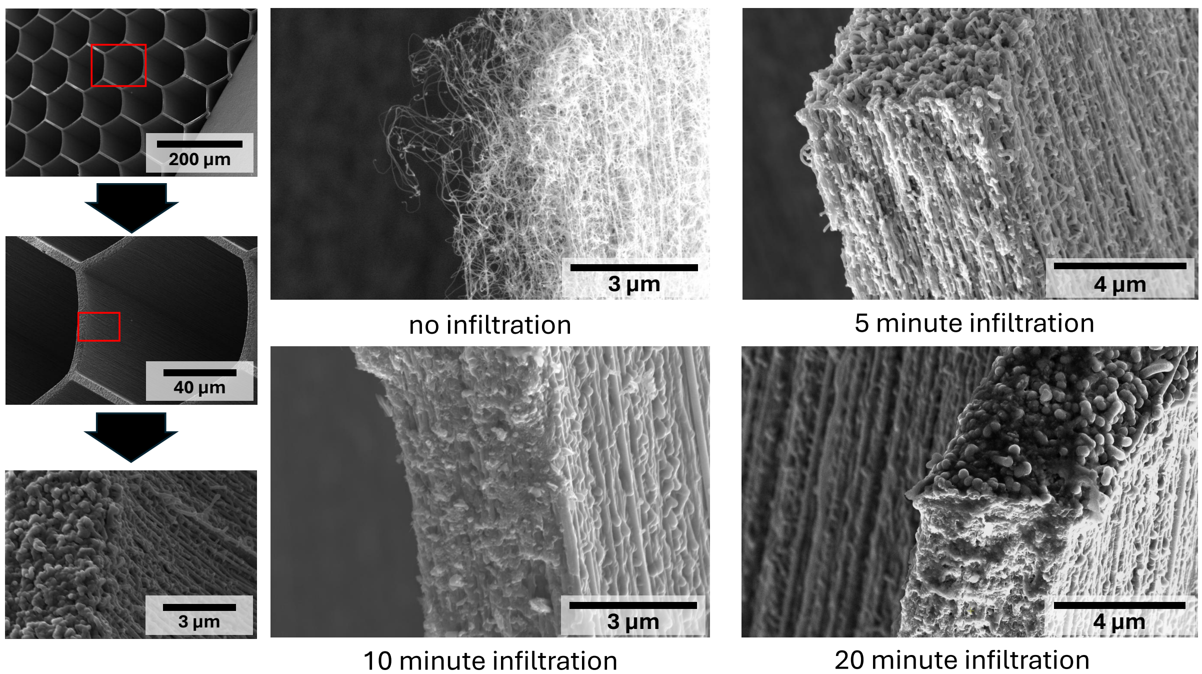

Figure 3.5 Cleaved cross sections of CNT collimators with different infiltration times (0, 5, 10, and 20 minutes).

Chapter 4

Simulation

Not all transmission through our optical apparatus will be recorded by the photodiode. When light makes a single reflection off the collimator's walls it's direction of travel changes. As the light travels to the photodiode, it's horizontal displacement increases. This can result in light transmitted through the CNT collimator not being recorded by the photodiode (see Fig. 4.1 (a)). However, light that has undergone an even numbered amount of reflections will exit the collimator at the same angle it entered at (see Fig. 4.1 (c)). This results in our measured data only picking up on even-numbered reflections, omitting light that had undergone odd-numbered reflections. We believe this is what caused the secondary peak/ side lobes for infiltrated CNT collimators in Fig. 3.1 and Fig. 3.3. These missed odd-reflection light rays can be detected by decreasing the distance between the CNT collimator and the light source (see Fig. 4.1 (b)). By creating a simulation where we decrease the distance between the CNT collimator and photodiode we can recover a more accurate transmission for infiltrated CNT collimators.

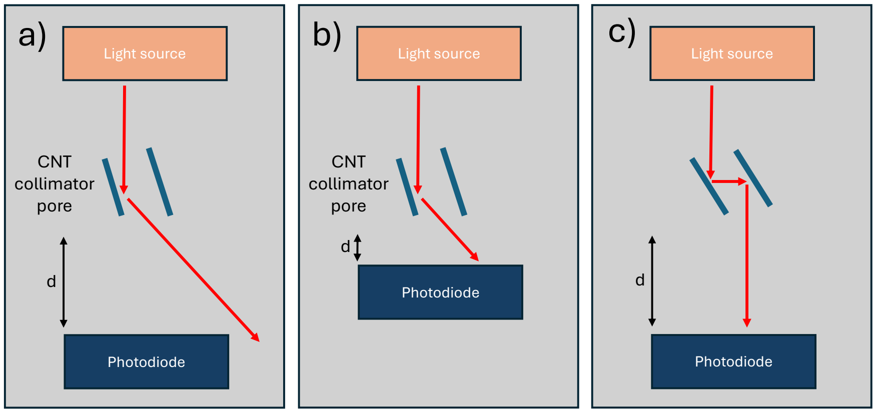

Figure 4.1 Schematic of a light ray traversing through a collimator pore. In (a) the light ray exiting after one reflection is at a different angle and goes too far to the side of the photo diode because the distance d is large. In (b) the light ray exiting after one reflection is measured by the photo diode with a shorter distance d. In (c) the light ray exiting after two reflections is measured by the photo diode with the larger distance d since it exited at the same angle at which it entered.

Depending on the application of the CNT collimator the distance between the CNT collimator and detector will vary. In our application of a spectrometer, the thickness of the LVF filter is minimal and thus the theoretical distance between the CNT collimator and photo diode is zero. By decreasing this distance in a simulation we can better approximate what the infiltrated collimator's light interaction will be for our the spectrometer.

The simulation takes incoming light and tracks its path through the same collimator geometry used in testing. A chosen number of initial light rays (3,000 in Fig.4.2) are evenly dispersed over the collimator's length. The length is porportional to the tested collimators, with 4 micron walls separating 26 parallel-hole wells; each 100 microns across (see Fig. 2.1).The height is set to 500 microns. The light rays then transverse through this geometry. When a ray comes in contact with a wall reflected (4.1), absorbed (4.2) and transmitted beams (4.3) are calculated and tracked throughout the rest of the collimator. These rays are calculated off of the absorption and transmission coefficients. Lastly, a set kill intensity of the initial ray is set to ensure the program will not go on forever.

$$\text{reflected percentage} = \left(\frac{n_1 - n_0}{n_1 + n_0}\right)^2 \tag{4.1}$$

$$\text{absorbed percentage} = 1 - e^{-\mu * \ell} \tag{4.2}$$

$$\text{transmitted percentage} = 1 - \text{reflected percentage} - \text{absorbed percentage} \tag{4.3}$$

n_0 and n_1 are the index of refraction for the material the ray starts in and going into. μ is the absorption coefficient, and ℓ is the path length the ray will have in the CNT wall.

The absorption and index of refraction are different for pristine and infiltrated CNT forests and therefore CNT collimators. The refractive index for infiltrated CNT forests is taken to be that of amorphous carbon: 2.4 [5, 6], for the pristine CNT collimators it is taken to be 1 [7, 8]. The absorption for pristine CNTs can be taken to be about 0.9 from literature [9–13]. For infiltrated CNT forests the refractive index is taken to be the same as amorphous carbon.

The model has a set distance from the collimator to the detector, allowing us to see multitudes of data we could've collected. We can decrease the distance d between the collimator and detector. The detector can then pick up on the single reflections that are not present in data taken.

As the distance to the detector increases the second and fourth reflections are isolated and begin to appear (see Fig. 4.2). Our recorded data for infiltrated collimators should be different from what was recorded, the actual integrated intensity would be different as well.

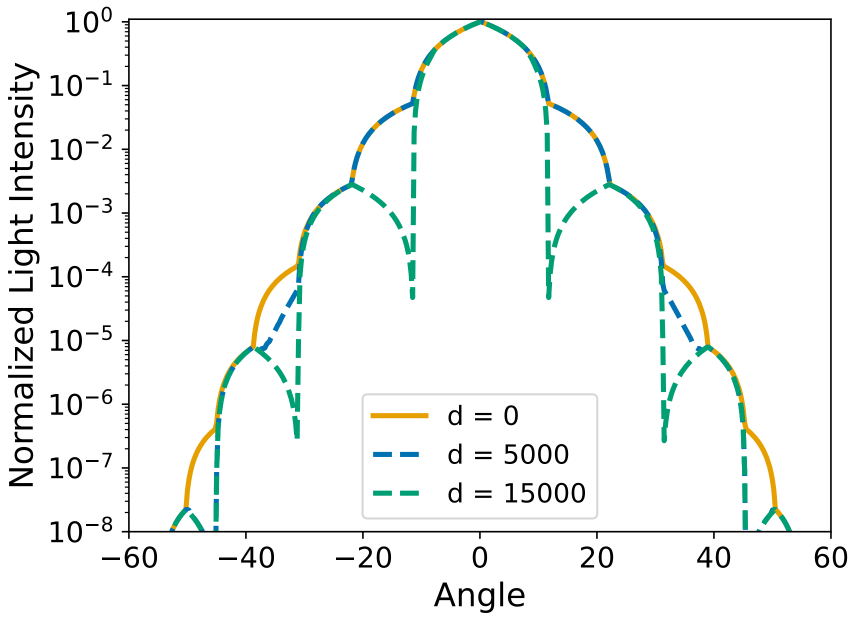

Figure 4.2 Modeled light interaction through a dense collimator with 100:500, pore:height ratio with varying distances to the detector.

Chapter 5

Analysis and Discussion

As seen in Fig.3.1 the pristine CNT collimator on the transparent substrate does not exhibit light that has undergone reflection. There is a waterfall attribute with the intensity falling off in intervals. These are a result of light needing to transmit through successive collimator walls. A simple equation from the collimator's geometry can be calculated that aligns with this waterfall effect.

The pristine collimator was grown to be 621 microns tall, and patterned with 100 micron wide pores, and 10 micron thick walls. The angle at which all light must pass at least n walls is

$$\theta_n = Arctan(\frac{n * \text{pore size} + (n-1) * \text{wall thickness}}{\text{wall height}}) \tag{5.1}$$

Plotting these θ_n on top of collected data taken for the pristine collimator gives,

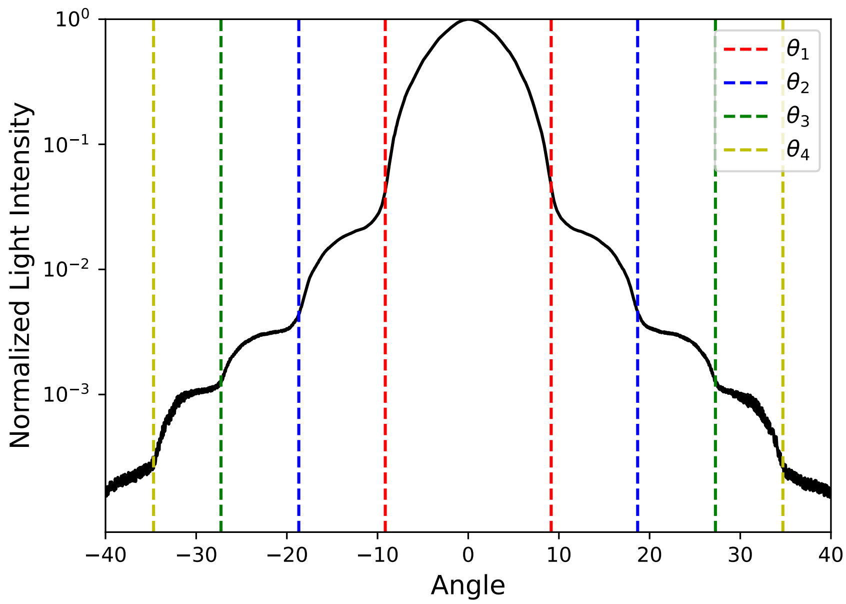

Figure 5.1 Pristine CNT collimator with transmission lines.For each angle greater than θ_n, light needs to travel through n walls to reach the detector.

Before each θ_n there is a sharp decrease in intensity due to the intensity dying as the light needs to transverse the n wall after θ_n to reach the detector. It is reassuring how the steep decreases occur are consistent along θ_n.

The side lobes for the infiltrated collimator can be predicted in a similar manner. The light that reaches the detector after the main peak needs to had undergone an even number of reflections as discuss in 4. Thus, another simple equation can be derived as above relying on the collimator's geometry to determine at what angle reflected light is expected.

$$\phi_n = Arctan(\frac{(1+2n) * \text{pore size}}{\text{wall height}}) \tag{5.2}$$

Below is a graph of the light interaction of a CNT collimator infiltrated for 20 minutes, grown to be 709 microns tall, and has a pore size of 100 microns.

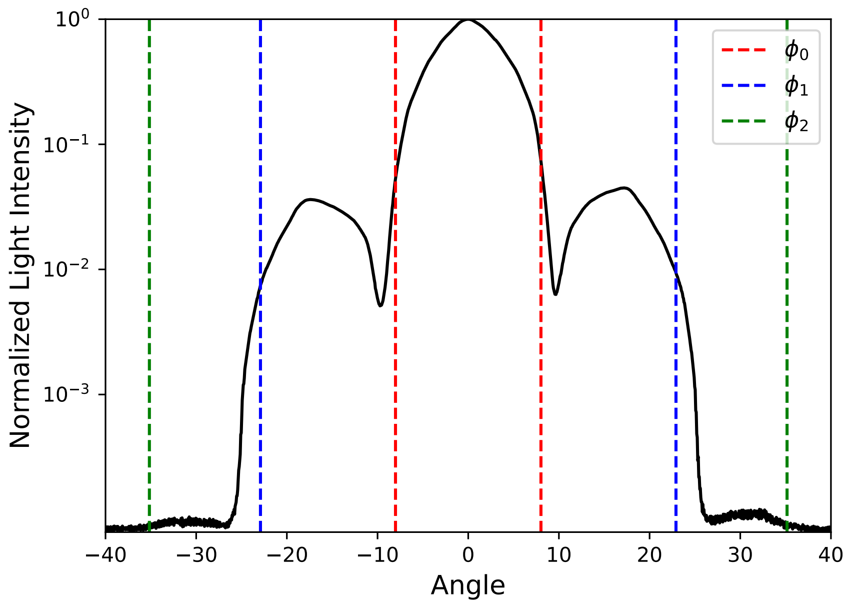

Figure 5.2 Infiltrated CNT collimator with reflection lines. ϕ_0 marks the cutoff of when light should be blocked off by the collimator wall. ϕ_1 and ϕ_2 mark the last angle light was able to make 2 and 4 reflections respectively.

In order to check for confirmation bias and that there was not another reason these features appeared, in section 4 a simulation was created.

It is still unknown when the transition between reflected and transmitted optical properties happen with our fabrication method. The infiltrated collimators are more dense and reflect light, this begs the question if there is a less thorough infiltration that leaves the CNT forests dense enough to not allow light to transmit but not too dense to make light reflect. When trying infiltration times short than 10 minutes the CNT structure become too fragile to handle with tweezers. A KOH etch can be used to remove the structure from the silicon substrate, but we are unable to place these collimators into the testing apparatus afterwards due to them breaking with tweezers.

The pristine CNT collimators grown on fused silica eliminate the inconveniences of further processing steps and remove evidence of reflected light but instill different problems. Although there

Infiltration Time	Height	Acceptance Angle	Significant Features	Integrated Intensity
0	621	8.38	13.3875*	0.1746
10	556	9.14	5.69E-03**	0.0249
15	787	7.90	1.08E-02**	0.0320
20	710	7.62	4.49E-02**	0.0934

Figure 5.3 Table of characteristics of CNT collimators taken from measured data. Acceptance angle it taken when intensity is 10% of maximum throughput, the integrated intensity is what fraction of the area outside the cutoff angle is. *Intensity of shoulder inflection point. ** Height of the second peak.

is high absorbance by the as-grown CNTs, there is an additional transmission through the sparse forest. By integrating the area under the transmission curve in Fig.3.1 and setting a cutoff angle we can compare between samples. By finding what area of the transmission curve is outside the cutoff angle we can see how well the collimator allows off-axis light to transmit. The integrated intensity outside a 10% cutoff angle for the pristine CNT collimator is 0.1746, double the integrated intensity of the 10-minute infiltrated CNT sample, 0.0934. The integrated intensity for infiltrated CNT collimators may be incorrect, however a 2x difference is difficult to overcome. The transmission through pristine CNT collimator could potentially mitigated with thicker sidewalls, though this would reduce the throughput of light through the collimator. In addition, pristine CNT collimators are less robust, only being practically handled with the fused silica substrate.

The acceptance angle can be controlled by the geometry of the patterned iron and the growth time for both fabrication methods. The height of the CNT collimator can be further controlled with the use of a laser. Being able to control these parameters then determines the light collimation.

The critical question of throughput was not considered. Because all recorded light interaction for the CNT collimators were normalized, throughput between collimators cannot be determined. I do not trust analyzing the non-normalized data, since our setup is not optimal to determine through put. Between runs there are slight differences in how collimators are attatched to the 3D printed piece, and how the laser is aligned as defined in section 2.2. There is adittional dependence on each CNT collimator: how well the carbon floor layer was etched, and deposition of loose carbon on the fused silica substrate could absord light. Throughput is valuable in the application to a LVF spectrometer since the more data that can make it to the detector, the more accurate spectroscopic readings will be.

Chapter 6

Conclusion

In this work we fabricated and characterized CNT collimators for diffuse light spectroscopy. CNT collimators were fabricated on both opaque silicon and transparent fused silica substrates. These collimators were then tested for light collimation. When tested for light collimation, infiltrated collimators had symmetrical side lobes around the expected central peak, while pristine collimators had a waterfall trait on both sides of the central peak.

We have demonstrated that CNT parallel-hole collimators exhibit distinct angular-transmission behaviors depending on infiltration. Pristine collimators on fused silica transmit light rays producing a "water fall" pattern. While infiltrated collimators suppress this transmission with thicker side walls and produce reflected rays. Thus rays that are detected by the photodiode are approaching at shallower angles. This is optimal for a LVF spectrometer since the filter relies on the light's path length for reflection in order to cancel out light rays. Acceptance angles can be changed with the collimator's geometer, wall thickness can be increased to decrease transmitted light. In general, micro-fabricated CNTs can be used to create a wide variety of NEMS and MEMS.

Bibliography

[1] T. Westover, Z. Westhoff, S. Poff, N. Morrill, D. Miller, S. Chiang, R. Vanfleet, and R. Davis, “Miniaturized short-wavelength infrared spectrometer for diffuse light applications,” Advanced Photonics Nexus 2 (2023).

[2] T. Westover, S. Olsen, Z. Westhoff, N. Morrill, R. Davis, and R. Vanfleet, “Visible and short-wavelength infrared light collimation through carbon nanotube, parallel-hole collimators,” Optics Express **30,** 22679 (2022).

[3] Zuidema, X. Ruan, and T. Fisher, “Optical properties of ordered carbon nanotube arrays grown in porous anodic alumina templates,” Optics Express **21,** 22053 (2013).

[4] “High surface-area carbon microcantilevers$_2$019,$'' Highsurface - areacarbonmicrocantilevers(2019)$.

[5] L. Skowronski, R. Chodun, M. Trzcinski, and K. Zdunek, “Optical Properties of Amorphous Carbon Thin Films Fabricated Using a High-Energy-Impulse Magnetron-Sputtering Technique,” Materials **16,** 7049 (2023).

[6] B. J. Stagg and T. T. Charalampopoulos, “Refractive indices of pyrolytic graphite, amorphous carbon, and flame soot in the temperature range 25° to 600°C,” Combustion and Flame **94,** 381–396 (1993).

[7] S. J. Park *et al.*, "Modulation of the effective density and refractive index of carbon nanotube forests via nanoimprint lithography," Carbon **129,** 8–14 (2018).

[8] H. Shi, J. G. Ok, H. Won Baac, and L. Jay Guo, "Low density carbon nanotube forest as an index-matched and near perfect absorption coating," Applied Physics Letters **99,** 211103 (2011).

[9] F. Kiani, F. Sterl, T. V. Tsoulos, K. Weber, H. Giessen, and G. Tagliabue, "Ultra-Broadband and Omnidirectional Perfect Absorber Based on Copper Nanowire/Carbon Nanotube Hierarchical Structure," ACS Photonics **7,** 366–374 (2020).

[10] K. Mizuno, J. Ishii, H. Kishida, Y. Hayamizu, S. Yasuda, D. N. Futaba, M. Yumura, and K. Hata, "A black body absorber from vertically aligned single-walled carbon nanotubes," Proceedings of the National Academy of Sciences **106,** 6044–6047 (2009).

[11] K. Laughlin, R. R. Vanfleet, and R. C. Davis, "Mechanically Robust Vertically Aligned Carbon Nanotube Composites for Applications in Ultralow Reflectance Optical Elements," ACS Applied Nano Materials **5,** 6989–6994 (2022).

[12] A. M. Gheitaghy, A. Ghaderi, S. Vollebregt, M. Ahmadi, R. Wolffenbuttel, and G. Q. Zhang, "Infrared absorbance of vertically-aligned multi-walled CNT forest as a function of synthesis temperature and time," Materials Research Bulletin **126,** 110821 (2020).

[13] F. De Nicola, C. Pintossi, F. Nanni, I. Cacciotti, M. Scarselli, G. Drera, S. Pagliara, L. Sangaletti, M. De Crescenzi, and P. Castrucci, "Controlling the thickness of carbon nanotube random network films by the estimation of the absorption coefficient," Carbon **95,** 28–33 (2015).